

EVIDENCE OF A FLAT OUTER ROTATION CURVE IN A STARBURSTING DISK GALAXY AT $Z = 1.6$

PATRICK M. DREW¹ , CAITLIN M. CASEY¹ , ANNE D. BURNHAM¹, CHAO-LING HUNG^{1,4}, SUSAN A. KASSIN^{3,2} ,
 RAYMOND C. SIMONS^{2,3} , AND JORGE A. ZAVALA¹ 

Draft version November 7, 2018

ABSTRACT

Observations of the baryon to dark matter fraction in galaxies through cosmic time are a fundamental test for galaxy formation models. Recent observational studies have suggested that some disk galaxies at $z > 1$ host declining rotation curves, in contrast with observations of low redshift disk galaxies where stellar or HI rotation curves flatten at large radii. We present an observational counterexample, a galaxy named DSFG850.95 at $z = 1.555$ (4.1 Gyr after the big bang) that hosts a flat rotation curve between radii of ~ 6 –14 kpc (1.2–2.8 disk scale lengths) and has a dark matter fraction of 0.44 ± 0.08 at the H-band half light radius, similar to the Milky Way. We create position-velocity and position-dispersion diagrams using Keck/MOSFIRE spectroscopic observations of H α and [NII] emission features, which reveal a flat rotation velocity of $V_{\text{flat}} = 285 \pm 12 \text{ km s}^{-1}$ and an ionized gas velocity dispersion of $\sigma_0 = 48 \pm 4 \text{ km s}^{-1}$. This galaxy has a rotation-dominated velocity field with $V_{\text{flat}}/\sigma_0 \sim 6$. Ground-based H-band imaging reveals a disk with Sérsic index of 1.29 ± 0.03 , an edge-on inclination angle of $87 \pm 2^\circ$, and an H-band half light radius of $8.4 \pm 0.1 \text{ kpc}$. Our results point to DSFG850.95 being a massive, rotationally-supported disk galaxy with a high dark-matter-to-baryon fraction in the outer galaxy, similar to disk galaxies at low redshift.

Subject headings: galaxies: kinematics and dynamics — galaxies: high-redshift — galaxies: evolution

1. INTRODUCTION

In the standard Λ CDM model of the Universe, the baryonic and dark matter components of galaxies grow in tandem from high to low redshift (e.g. White & Rees 1978). Galactic rotation curves are an important observational probe of these matter distributions in galaxies (see Sofue & Rubin 2001, for a brief review). Through Keplerian inference, rotation curves provide a direct method for measuring the mass enclosed within a galactocentric radius. When combined with a light profile and a mass-to-light ratio, one may estimate the distribution of dark matter in a galaxy (e.g. Carignan & Freeman 1985; van Albada et al. 1985; Kassin et al. 2006; de Blok et al. 2008; Korsaga et al. 2018).

At low redshift (z), disk galaxy rotation curves are seen to rise sharply in the inner few kpc and then flatten to a near-constant velocity (e.g. Rubin et al. 1978; McGaugh 2016). This is caused by baryons dominating the mass density in the inner regions of galaxies while dark matter dominates in the outer regions (Kassin et al. 2006; Courteau et al. 2007; Dutton et al. 2007; Barnabè et al. 2012; Cappellari et al. 2013; Dutton et al. 2013; Martinsson et al. 2013a,b; Courteau & Dutton 2015). Recent observational studies have begun to push galaxy rotation curve measurements to larger radii at $z \gtrsim 1$ and while some find flat rotation curves (e.g. Di Teodoro et al. 2016, 2018; Xue et al. 2018), others, intriguingly, find evidence

of decreasing outer-galaxy rotation curves (Lang et al. 2017; Genzel et al. 2017). These studies attribute this to a combination of decreased dark matter in galaxies at intermediate redshifts as well as increased pressure support in the outer disks. It is common for low redshift disk galaxies to show an initial decline before flattening in the outer disk (e.g. Rubin et al. 1965, 1978; McGaugh 2016), but the low or negligible inferred dark-matter-to-total mass fractions in the Lang et al. and Genzel et al. samples imply that these initial declines will not begin to flatten if detected at higher radii.

Some studies find lower dark matter fractions in galaxies at $z \gtrsim 1$ than at $z = 0$ (Förster Schreiber et al. 2009; Price et al. 2016; Burkert et al. 2016; Wuyts et al. 2016) while others find no evolution (Stott et al. 2016; Yuan et al. 2017; Di Teodoro et al. 2016). Many of these works rely on inverting scaling relations with significant scatter, such as the Kennicutt-Schmidt relation (Kennicutt 1998), in order to estimate gas masses. This may be the source of disagreement. There is much greater agreement among many of these studies when comparing the stellar to the total masses of the galaxies (See also Pelliccia et al. 2017).

Different simulations also make different predictions about the shapes of rotation curves at $z > 1$. Teklu et al. (2018) find 38% of disk galaxies with $M_\star > 5 \times 10^{10} M_\odot$ at $z = 2$ in the cosmological hydrodynamic simulation, *Magneticum Pathfinder* (K. Dolag et al., in preparation) have declining rotation beyond $\sim 4 \text{ kpc}$ (as estimated from Figure 4 in Teklu et al. 2018). In contrast, the IllustrisTNG cosmological hydrodynamic simulations (Lovell et al. 2018) show initially declining rotation curves at $z = 2$ that gradually flatten in the outer disk, similar to low- z disk galaxies. It is clear that more observations of the outer rotation curves of high redshift galaxies and their dark matter fractions are needed to puzzle out the

Email: pdrew@utexas.edu

¹ Department of Astronomy, The University of Texas at Austin, 2515 Speedway Blvd Stop C1400, Austin, TX 78712

² Johns Hopkins University, Baltimore, 3400 North Charles St., MD, 21218, USA

³ Space Telescope Science Institute, 3700 San Martin Dr., Baltimore, MD, 21218, USA

⁴ Department of Physics, Manhattan College, 4513 Manhattan College Pkwy Bronx, NY 10471

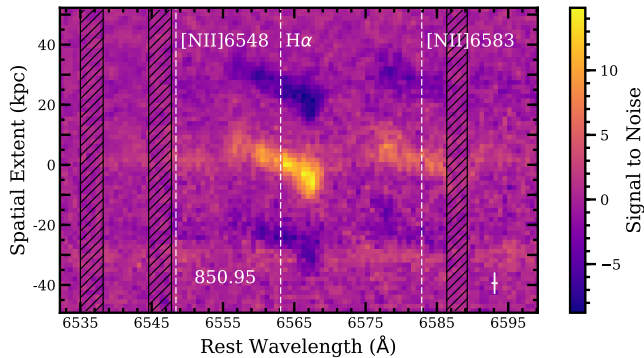


FIG. 1.— Two dimensional signal-to-noise spectrum of DSFG850.95 showing $H\alpha$, [NII], and continuum emission showing symmetric rotation with a flattened rotational velocity at high galactocentric radii. Hatched regions denote pixels significantly contaminated by telluric sky emission. Vertical dashed lines mark the location of $H\alpha$, [NII] λ 6548, and [NII] λ 6583. The white cross represents the resolution in each dimension. Negative reflections of the spectrum are caused by the standard ABBA nodding pattern used. A separate foreground source at $z = 0.7$ sits at a projected radius of ~ 30 kpc to the south of DSFG850.95 and is the source of continuum emission seen toward the bottom of the 2D spectrum.

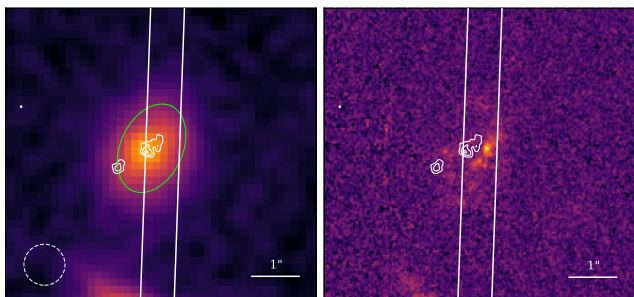


FIG. 2.— Imaging of DSFG850.95 in H band (Left; rest-frame 6400 Å; McCracken et al. 2012) and *HST* F814W (Right; rest-frame 3200 Å; Koekemoer et al. 2007) with the MOSFIRE slit and ALMA dust contours at 3, 4, and 5 σ significance (Burnham et al. in preparation) in white. The white dashed circle shows the FWHM of seeing for the MOSFIRE observations. The green ellipse shows the H-band half-light radius. Emission seen to the south is from an unrelated foreground galaxy at a photometric redshift of 0.7.

evolution of dark matter fractions with time.

In this paper we present the serendipitously acquired rotation curve for a known dusty star forming galaxy at $z = 1.555$, detected in $H\alpha$ to a high galactocentric radius of 14 kpc. The galaxy exhibits a flat rotation curve, well-fit by an arctangent profile and a dark matter fraction at 14 kpc typical of disk galaxies at $z = 0$. The paper is organized as follows. Section 2 details the observations and data reduction, Section 3 discusses the kinematic modeling, Section 4 details the dynamical and stellar mass estimations, and Section 5 presents our conclusions. Throughout this work we adopt a *Planck* cosmology with $H_0 = 67.7 \text{ km s}^{-1} \text{ Mpc}^{-1}$ and $\Omega_\Lambda = 0.6911$ (Planck Collaboration et al. 2016). We assume a Chabrier initial mass function (IMF; Chabrier 2003).

2. OBSERVATIONS AND DATA REDUCTION

The data were obtained with the Multi-Object Spectrometer For Infra-Red Exploration (MOSFIRE; McLean et al. 2010, 2012) on Keck I as part of an observational campaign to follow up a sample of 450 μm - and

850 μm -identified dusty star forming galaxies (DSFGs; for sample details see Casey et al. 2013, 2017). DSFGs comprise the most intense star-bursting galaxies in the Universe (See reviews by Blain et al. 2002 and Casey, Narayanan, & Cooray 2014).

Observations were made on 2013 December 31 with the full width at half maximum (FWHM) of seeing between $0''.8$ – $0''.9$, as measured by the telescope focus routine, MIRA. We adopt an average seeing of $0''.85$ throughout this work. The galaxy, DSFG850.95, was observed in the H band for a total integration time of 1920 s with the slit width set to $0''.7$. An $1''.5$ ABBA nod pattern was used and the slit orientation was randomly placed with respect to our target due to position angle optimization driven by multiplexing. Additional observational details are described for the full parent sample in Casey et al. (2017).

The data were reduced with the MOSPY data reduction pipeline⁵. Figure 1 plots the reduced 2D signal to noise spectrum of DSFG850.95 showing $H\alpha$, [NII], and continuum emission. An unrelated foreground galaxy at photometric redshift of 0.7, COSMOS 2004241 (Capak et al. 2007), sits a projected $\sim 3''.5$ to the south of DSFG850.95 and is seen in faint continuum emission in Figure 1 at spatial extent ~ 30 kpc. It does not affect the analysis of DSFG850.95’s rotation curve.

The left panel of Figure 2 shows H-band imaging (rest-frame ~ 6400 Å), MOSFIRE slit, and ALMA 870 μm dust continuum contours of DSFG850.95. The H-band FWHM of seeing was comparable to that of the MOSFIRE observations and is shown as the dashed circle. The green ellipse shows the H-band half-light radius. There is a misalignment between the position angles of the H-band exponential disk fit and the slit of $23 \pm 4^\circ$, which should not strongly affect our measured radial velocities. We will discuss this further in subsection 3.1. The right panel of Figure 2 shows *Hubble* imaging in the F814W filter, at a rest-frame effective wavelength of ~ 3200 Å. The centroid of UltraVISTA K-band emission was used for the slit targeting position (rest-frame ~ 8600 Å). It shares the same positional centroid as the H-band image in the left panel of Figure 2, however the slit was slightly offset from the intended target position. The seeing on the night of the MOSFIRE observation is much larger than this offset, and is large enough to cause emission originating from positions outside the slit to be probed by the slit. This offset, therefore, does not strongly affect our analysis. Additionally, the rest-frame UV emission, which expected to originate in the same regions as the $H\alpha$ emission is well-probed by the slit, though it is more highly extinguished than the $H\alpha$ emission. The offset between the *HST* and dust emission centroids does demonstrate the importance of dust obscuration in this dusty star forming galaxy, however. Figure 3 shows another look at the *HST* I-band imaging in blue with ALMA 870 μm dust continuum in red.

We extracted 1D spectra from the MOSFIRE data using the IRAF⁶ routine APALL. Apertures of extraction

⁵ <http://keck-datareductionpipelines.github.io/MosfireDRP/>

⁶ IRAF is distributed by the National Optical Astronomy Observatories, which are operated by the Association of Universities for Research in Astronomy, Inc., under cooperative agreement with the National Science Foundation

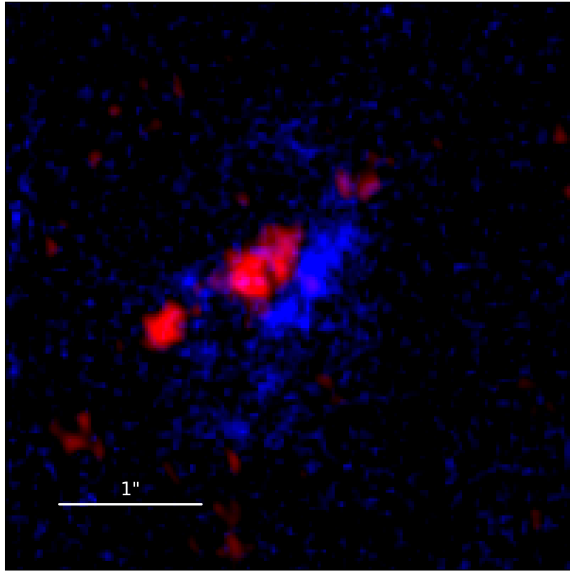


FIG. 3.— Imaging of DSFG850.95 in *HST* F814W (rest-frame UV) and ALMA 870 μm dust continuum at $0''.1$ resolution in blue and red respectively.

were placed on each pixel across the galaxy with a radius equal to half the average seeing. Spectra were extracted with variance weighting. Radial velocities and velocity dispersions were measured from the extracted spectra using the SPLOT fitting routine in IRAF. We fit H α , [NII] λ 6548, and [NII] λ 6583 simultaneously with fixed spacing between spectral features and tied but variable emission line full widths at half maximum (FWHM). Pixels contaminated with telluric line emission were omitted from the fits and errors in the best-fit parameters were estimated using 1000 Monte Carlo perturbations of the data by typical sky noise. Figure 4 shows the position-velocity and position-dispersion diagrams measured from these fits. The velocity curve (upper panel), corrected for galaxy inclination angle (see subsection 3.1 for details), rises steeply in the inner few kpc and then flattens to a near-constant velocity in the outer regions of the galaxy. The dispersion curve (lower panel) is centrally peaked due to the effect of beam smearing.

3. KINEMATIC MODEL

We model the rotational velocity, $V(r)$, and velocity dispersion, $\sigma(r)$ of DSFG850.95 following the method employed by e.g. Courteau (1997); Weiner et al. (2006), modified to allow for the parameterization of a possible decline in rotational velocity at high galactocentric radii. The model assumes the intrinsic rotation curve follows a modified arctan function of the form:

$$V(r) = \frac{2}{\pi} V_a \arctan\left(\frac{r}{r_t}\right) + cr, \quad (1)$$

where V_a is the asymptotic velocity, r_t is the knee radius, r is the distance from the center of the galaxy, and c is the outer-galaxy slope which allows us to quantify the degree to which the rotation curve increases, flattens, or decreases.

We also measure an isotropic ionized gas velocity dispersion for the entire galaxy, σ_0 , which is taken to be the vertical offset of a Gaussian fitted to the position-

TABLE 1
PHYSICAL CHARACTERISTICS OF DSFG850.95

PROPERTY	VALUE
z	1.555
V_{flat}^a	$285 \pm 12 \text{ km s}^{-1}$
σ_0	$48 \pm 4 \text{ km s}^{-1}$
V_{flat}/σ_0	6
$\Delta\text{P.A.}^b$	$23 \pm 4^\circ$
n^c	1.29 ± 0.03
i^d	$87 \pm 2^\circ$
$r_{1/2}$	$8.4 \pm 0.1 \text{ kpc}$
$r_{2.2}$	$11.0 \pm 0.2 \text{ kpc}$
r_{max}^e	14.1 kpc
SFR	$280^{+110}_{-90} \text{ M}_\odot \text{ yr}^{-1}$
M_*	$(3.8 \pm 3.0) \times 10^{10} \text{ M}_\odot$
M_{H_2}	$(8.88 \pm 0.03) \times 10^{10} \text{ M}_\odot$
$M_{\text{dyn}}(14 \text{ kpc})$	$(2.7 \pm 0.3) \times 10^{11} \text{ M}_\odot$
$M_{\text{dyn}}(R_{1/2})$	$(1.9 \pm 0.1) \times 10^{11} \text{ M}_\odot$
$f_{\text{DM}}(R_{1/2})$	0.44 ± 0.08

^aAverage of flat rotation on both sides of DSFG850.95.

^bPosition angle offset between slit and H-band semi-major axis.

^cSérsic Index.

^dInclination angle.

^eMaximum detected radius of H α .

dispersion data in the bottom panel of Figure 4:

$$\Sigma(r) = A \exp\left(-\frac{(r-m)^2}{2w^2}\right) + \sigma_0, \quad (2)$$

where $\Sigma(r)$ is the value of the fitted Gaussian at each r , A is the amplitude, r is the distance from the center of the galaxy, m is the central position, w is the width of the Gaussian, and σ_0 is the isotropic velocity dispersion. We choose σ_0 as the representative dispersion for DSFG850.95 because it is the value the velocity dispersion approaches in the outer galaxy where beam smearing has less of an effect. Beam smearing is well known to artificially increase the observed velocity dispersion toward the centers of galaxies due to the rise in the rotation curve (e.g. Bosma 1978; Weiner et al. 2006; Di Teodoro & Fraternali 2015), but has less of an effect at higher galactocentric radii.

We correct the observed velocity dispersions for the intrinsic instrumental dispersion prior to fitting using the equation: $\sigma = \sqrt{\sigma_{\text{obs}}^2 - \sigma_{\text{inst}}^2}$ where σ is the velocity dispersion reported in Figure 4, σ_{obs} is the FWHM of the emission line divided by 2.355 and σ_{inst} is the combined instrumental and spectral seeing dispersion, taken to be the average width of several telluric lines measured across the unredshifted spectrum ($\sigma_{\text{inst}} = 39 \pm 2 \text{ km s}^{-1}$). The reported error on σ_{inst} is the standard deviation in the mean of the measured telluric line widths and are folded into the errors in velocity dispersion in Figure 4. Measured velocity dispersions that are less than the instrumental dispersion are unreliable because small errors on the observed dispersion correspond to large changes in the inferred physical dispersion (Weiner et al. 2006). Dispersions measured below the instrumental seeing are plotted as upper limits at 2σ significance in the bottom panel of Figure 4 and are excluded from the dispersion curve fits, though their central wavelengths are still fitted for the velocity curve.

We fit the position-velocity and position-dispersion data with the pymc3 python package for Markov Chain Monte Carlo (MCMC; Salvatier et al. 2016) so that we

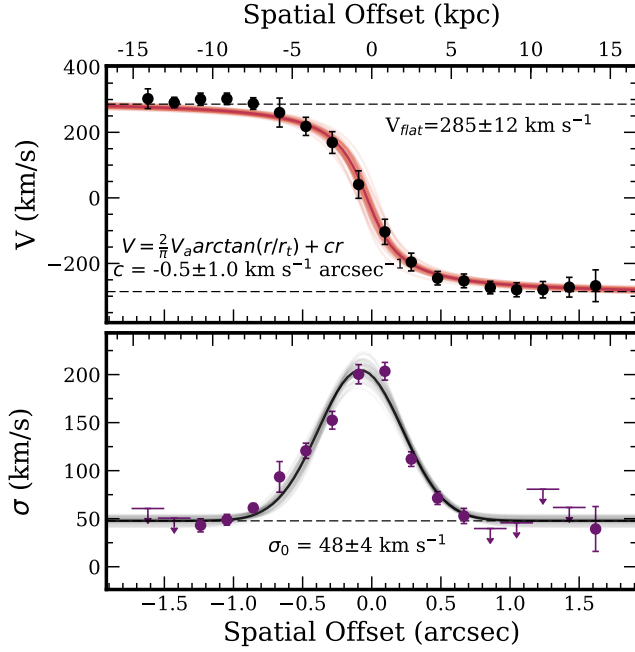


FIG. 4.— Position-velocity and position-dispersion diagrams of DSFG850.95 showing flattened rotation between ~ 6 – 14 kpc with average velocity of $V_{\text{flat}} = 285 \pm 12 \text{ km s}^{-1}$, marked as the dashed lines in the upper panel. The light red curves show 50 randomly-selected Monte Carlo chains from the velocity curve fit with the dark red curve showing the best fit. The outer-galaxy slope of $c = -0.5 \pm 1.0 \text{ km s}^{-1} \text{ arcsec}^{-1}$ is consistent with flat rotation. The grey curves show 50 randomly-selected Monte Carlo chains from the dispersion fit and the black curve shows the best fit with galaxy-wide ionized gas velocity dispersion of $\sigma_0 = 48 \pm 4 \text{ km s}^{-1}$, marked as the dashed line in the lower panel, implying DSFG850.95 is rotation dominated ($V_{\text{flat}}/\sigma_0 \approx 6$). Rotational velocities are measured from spectral extraction apertures centered on each pixel in the 2D spectrum with a radius of half the average seeing and are corrected for a galaxy inclination of $i = 87 \pm 2^\circ$. Upper limits on the velocity dispersion are at 2σ significance where the measured dispersion is less than the combined instrumental and seeing dispersion as measured from telluric line widths.

may characterize the posterior probability distributions of our fit parameters. The light red curves in the top panel of Figure 4 show fifty randomly-chosen MC fits and the best-fit curve is plotted in dark red. The best-fit value of asymptotic velocity is $|V_a| = 310 \pm 6 \text{ km s}^{-1}$, the knee radius is $r_t = 0''.17 \pm 0''.02$ or $1.5 \pm 0.2 \text{ kpc}$, and the outer slope is $c = -0.5 \pm 1.0 \text{ km s}^{-1} \text{ arcsec}^{-1}$, which is consistent with a flat slope. The best-fit velocity curve is still seen to be rising at the radius of the outermost datapoint. There is no evidence of a velocity turnover with declining rotation. The average velocity of the flat portion, taken to be the average of the datapoints between radii of ~ 6 – 14 kpc , corresponding to 1.2 – 2.8 disk scale lengths, is $V_{\text{flat}} = 285 \pm 12 \text{ km s}^{-1}$.

The bottom panel of Figure 4 shows the measured velocity dispersion data with fifty randomly-selected MC fits overplotted in grey with the best-fit curve in black. The best-fit dispersion, σ_0 , is $48 \pm 4 \text{ km s}^{-1}$, typical of mildly turbulent disk galaxies at $z \sim 1.5$ (e.g. Wright et al. 2007; Law et al. 2009; Epinat et al. 2012; Contini et al. 2012; Wisnioski et al. 2015; Simons et al. 2017).

3.1. H-Band Light Profile Fitting

Using the 2D image fitting code, GALFIT (Peng et al. 2002), we fit a Sérsic profile (Sérsic 1963) to H-band

imaging of DSFG850.95 from the UltraVISTA survey (McCracken et al. 2012, see Figure 2, above).

The fit reveals a Sérsic index of $n = 1.29 \pm 0.03$, implying an exponential disk light profile. Adding a second Sérsic component to fit a bulge causes significantly worse fits. The H-band half-light radius is $r_{1/2} = 8.4 \pm 0.1 \text{ kpc}$, or using the relation $r_d = r_{1/2}/1.68$, the disk scale radius is $r_d = 5.0 \pm 0.1 \text{ kpc}$ and $r_{2.2} = 11.0 \pm 0.2 \text{ kpc}$. We divide the velocities in the top panel of Figure 4 by $\sin(i)$ to correct for galaxy inclination, assuming an intrinsic edge-on axis ratio of 0.25 (Wuyts et al. 2016). From our best-fit axis ratio, $b/a = 0.668 \pm 0.008$, we determine the galaxy has an approximately edge-on inclination of $i = 87 \pm 2^\circ$ using the equation (e.g. Wuyts et al. 2016):

$$\cos i = \sqrt{\frac{(b/a)^2 - 0.25^2}{1 - 0.25^2}} \quad (3)$$

Table 1 summarizes the physical characteristics of DSFG850.95 from GALFIT and our other analyses.

There is a misalignment of $23 \pm 4^\circ$ between the position angles of the H-band semi-major axis and the slit. Large misalignments would result in an underprediction of the maximum rotational velocity of a galaxy, however Weiner et al. (2006) shows that the average decrease in observed rotational velocities for a slit misalignment of $\sim 23^\circ$ is small — approximately the same as the error on our measurement of V_{flat} .

The H-band imaging, together with the rotational velocity and velocity dispersion analyses in section 3 suggest DSFG850.95 is a rotationally-dominated disk galaxy at $z = 1.555$ that is similar to massive disk galaxies at low redshift.

4. DYNAMICAL, STELLAR, GAS, AND DARK MATTER MASSES

Our radial velocity measurements as a function of radius, corrected for galaxy inclination and ionized gas velocity dispersion support allow us to measure the total mass enclosed as a function of radius in the galaxy using the equation (e.g. Erb et al. 2003; Swinbank et al. 2004; van Starkenburg et al. 2008; Epinat et al. 2009; Di Teodoro et al. 2018):

$$M_{\text{dyn}}(r) = \frac{V_c^2(r)r}{G}, \quad (4)$$

where G is the gravitational constant, r is the galactocentric radius, and V_c is the circular velocity, given by:

$$V_c = \sqrt{V^2 + 2\sigma_0^2 \frac{r}{r_d}}, \quad (5)$$

where V is the inclination-corrected rotational velocity, σ_0 (measured to be $48 \pm 4 \text{ km s}^{-1}$) is the isotropic ionized gas velocity dispersion, and r_d is the exponential disk scale length measured from H-band imaging. The median difference between the rotational and circular velocities is 2%, since σ_0 is small compared to V .

The top panel of Figure 5 shows the dynamical mass as a function of radius. The total dynamical mass enclosed within the H-band half light radius is $(1.9 \pm 0.1) \times 10^{11} M_\odot$, and within 14 kpc is $(2.7 \pm 0.3) \times 10^{11} M_\odot$. The horizontal dashed line and shaded region in the top panel of Figure 5 marks the maximum dynamical mass and its

associated error. The bottom panel of Figure 5 shows the fraction of dynamical mass enclosed by radius.

Next we compare the dynamical mass at the half light radius with stellar and gas masses. Casey et al. (2017) uses MAGPHYS with the high- z extension (da Cunha et al. 2008, 2015) to fit UV through sub-mm ancillary photometry from the COSMOS collaboration (Capak et al. 2007; Laigle et al. 2016) and finds a stellar mass of $M_\star = (3.8^{+0.4}_{-1.0}) \times 10^{10} M_\odot$. We follow the procedure of Hainline et al. (2011) for similarly-selected DSFGs at similar redshifts to derive a more conservative error than Casey et al. We take the error to be half the difference between the stellar mass estimated with an instantaneous burst history and that estimated with a continuous star formation history. Thus, we arrive at a total stellar mass of $M_\star = (3.8 \pm 3.0) \times 10^{10} M_\odot$. Table 1 summarizes all the estimated and measured parameters of this galaxy.

Following the prescription of Scoville et al. (2016) we use our ALMA 870 μm dust continuum observations to estimate a molecular gas mass of $(8.9 \pm 0.4) \times 10^{10} M_\odot$, all of which is contained within the half light radius. We calculate the dark matter fraction at the half light radius using the equation:

$$f_{\text{DM}}(R_{1/2}) = 1 - \frac{M_\star(R_{1/2}) + M_{\text{gas}}}{M_{\text{dyn}}(R_{1/2})}, \quad (6)$$

where $M_\star(R_{1/2})$ is half of the total stellar mass, M_{gas} is the gas mass, and $M_{\text{dyn}}(R_{1/2})$ is the dynamical mass at the half light radius. We find $f_{\text{DM}}(R_{1/2}) = 0.44 \pm 0.08$. Figure 6 shows the dark matter fraction as a function of circular velocities for a few studies in the literature (Martinsson et al. 2013a,b; Bland-Hawthorn & Gerhard 2016; Genzel et al. 2017). DSFG850.95 has a dark matter fraction closer to that of the Milky Way than the galaxies in Genzel et al. (2017), though it has a higher rotational velocity than the Milky Way.

We conclude by noting that our finding of a flat rotation curve may not be inconsistent with the conclusions of Lang et al. (2017). The majority of disk galaxies in cosmological hydrodynamic simulations by Teklu et al. (2018) exhibit flat rotation curves with only 38% hosting declining rotation curves. Lang et al. (2017) split their data out into two subsamples according to the degree of pressure support, one with $V_{\text{rot}}/\sigma_0 > 6.3$ and the other < 6.3 . They define V_{rot} as the intrinsic, inclination corrected peak rotation velocity and σ_0 as the intrinsic velocity dispersion, both equivalent to our V_c and σ_0 . The galaxies with less pressure support ($V_{\text{rot}}/\sigma_0 > 6.3$) have flatter outer rotation curves than those with more pressure support, supporting the conclusion that much of the observed velocity decrease in their sample is due to increased pressure support. Our rotation curve, with a $V_c/\sigma_0 \sim 6$ is consistent with their stacked curve of galaxies with $V_{\text{rot}}/\sigma_0 > 6.3$. A statistical sample of galaxy rotation curves detected well beyond 10 kpc is needed to determine the fraction of flat or declining rotation curves at high redshift.

5. SUMMARY

Recent observations of disk galaxy rotation curves have found declining rotational velocities beyond ≈ 2.2 exponential disk scale lengths, implying intermediate redshift

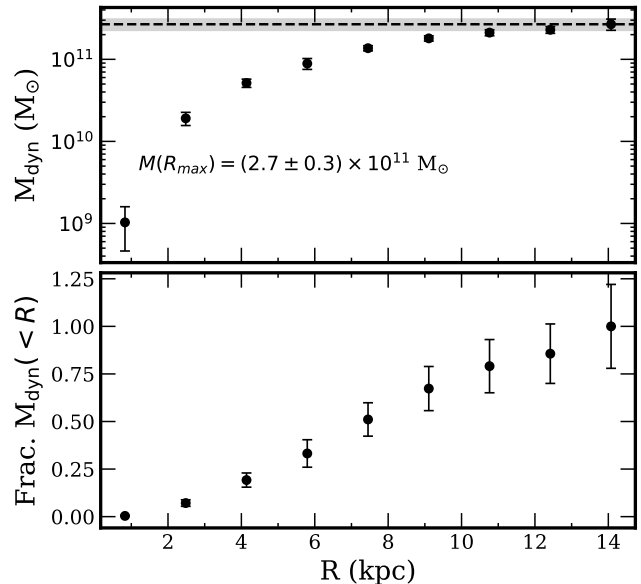


FIG. 5.— Top: The dynamical mass as a function of radius using $M_{\text{dyn}} = V_c^2(R)R/G$, where V_c is the circular velocity, R is radius, and G is the gravitational constant. The horizontal black dotted line is the dynamical mass at the largest radius, ~ 14 kpc, and the grey shaded region denotes the extent of the errors on that measurement. Datapoints are the average from both sides of the galaxy. Bottom: The fraction of dynamical mass enclosed as a function of galactocentric radius.

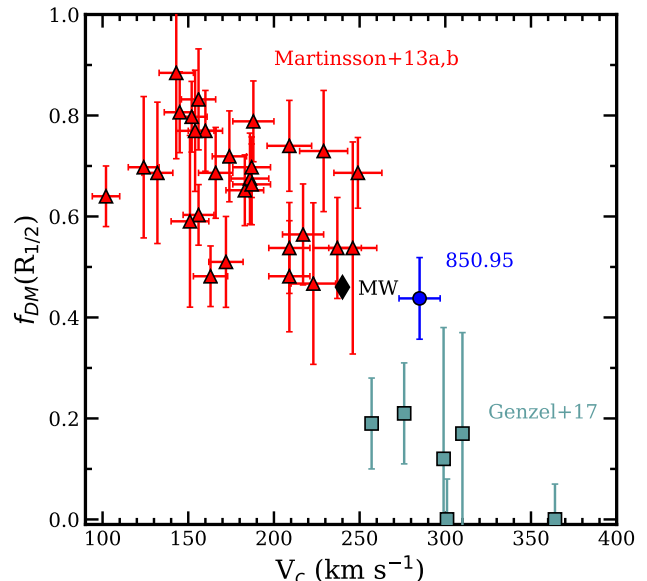


FIG. 6.— The fraction of dark matter at the half light radius as a function of circular velocity at the half light radius for different samples in the literature. The red triangles show $z = 0$ disk galaxies (Martinsson et al. 2013a,b), the Milky Way is plotted as the black diamond (Bland-Hawthorn & Gerhard 2016), and the Genzel et al. (2017) sample is plotted as light blue squares. The dark matter fraction of DSFG850.95 is more similar to that of the Milky Way, albeit at a higher circular velocity.

disk galaxies have lower dark matter fractions than $z = 0$ galaxies as well as increased velocity dispersion support.

In this paper we present a clear counterexample from MOSFIRE observations of H α and [NII] emission in the $z = 1.555$ disk galaxy, DSFG850.95, showing a flat rotation curve between ~ 6 –14 kpc (1.2–2.8 disk scale

lengths), well-fit by an arctangent function. At the H-band half light radius we estimate the dark matter fraction to be 0.44 ± 0.08 based on UV-through-sub-mm photometry and $870 \mu\text{m}$ dust continuum observations. Ground-based H-band imaging reveals a sersic index of $n = 1.29 \pm 0.03$ and an edge-on inclination angle. Taken together, these data suggest DSFG850.95 is a massive, rotationally supported disk galaxy in place by $z = 1.555$ (4.1 Gyr after the big bang) with a flat rotation curve and a dark matter fraction at the half light radius, similar to low redshift disk galaxies.

The authors thank the anonymous referee for a constructive report that significantly strengthened the arguments presented in this paper. The authors also wish to thank Michael Boylan-Kolchin, Michael Petersen, and Justin Spilker for useful discussions. P.M.D. and C.M.C.

acknowledge financial support from NASA Keck PI Data Awards: 2012B-U039M, 2011B-H251M, 2012B-N114M, 2017A-N136M, the University of Texas at Austin College of Natural Sciences, and NSF grants AST-1714528 and AST-1814034. This paper makes use of ALMA data ADS/JAO.ALMA#2015.1.00568S. ALMA is a partnership of ESO (representing its member states), NSF (USA) and NINS (Japan), together with NRC (Canada) and NSC and ASIAA (Taiwan) and KASI (Republic of Korea), in cooperation with the Republic of Chile. The Joint ALMA Observatory is operated by ESO, AUI/NRAO and NAOJ. The authors wish to recognize and acknowledge the very significant cultural role and reverence that the summit of Mauna Kea has always had within the indigenous Hawaiian community. We are most fortunate to have the opportunity to conduct observations from this mountain.

REFERENCES

- Barnabè, M., Dutton, A. A., Marshall, P. J., et al. 2012, *MNRAS*, 423, 1073
- Blain, A. W., Smail, I., Ivison, R. J., Kneib, J.-P., & Frayer, D. T. 2002, *Phys. Rep.*, 369, 111
- Bland-Hawthorn, J., & Gerhard, O. 2016, *ARA&A*, 54, 529
- Bosma, A. 1978, PhD thesis, PhD Thesis, Groningen Univ., (1978)
- Burkert, A., Förster Schreiber, N. M., Genzel, R., et al. 2016, *ApJ*, 826, 214
- Capak, P., Aussel, H., Ajiki, M., et al. 2007, *ApJS*, 172, 99
- Cappellari, M., McDermid, R. M., Alatalo, K., et al. 2013, *MNRAS*, 432, 1862
- Carignan, C., & Freeman, K. C. 1985, *ApJ*, 294, 494
- Casey, C. M., Narayanan, D., & Cooray, A. 2014, *Phys. Rep.*, 541, 45
- Casey, C. M., Chen, C.-C., Cowie, L. L., et al. 2013, *MNRAS*, 436, 1919
- Casey, C. M., Cooray, A., Killi, M., et al. 2017, *ApJ*, 840, 101
- Chabrier, G. 2003, *PASP*, 115, 763
- Contini, T., Garilli, B., Le Fèvre, O., et al. 2012, *A&A*, 539, A91
- Courteau, S. 1997, *AJ*, 114, 2402
- Courteau, S., & Dutton, A. A. 2015, *ApJ*, 801, L20
- Courteau, S., Dutton, A. A., van den Bosch, F. C., et al. 2007, *ApJ*, 671, 203
- da Cunha, E., Charlot, S., & Elbaz, D. 2008, *MNRAS*, 388, 1595
- da Cunha, E., Walter, F., Smail, I. R., et al. 2015, *ApJ*, 806, 110
- de Blok, W. J. G., Walter, F., Brinks, E., et al. 2008, *AJ*, 136, 2648
- Di Teodoro, E. M., & Fraternali, F. 2015, *MNRAS*, 451, 3021
- Di Teodoro, E. M., Fraternali, F., & Miller, S. H. 2016, *A&A*, 594, A77
- Di Teodoro, E. M., Grillo, C., Fraternali, F., et al. 2018, *MNRAS*, arXiv:1801.06546
- Dutton, A. A., van den Bosch, F. C., Dekel, A., & Courteau, S. 2007, *ApJ*, 654, 27
- Dutton, A. A., Treu, T., Brewer, B. J., et al. 2013, *MNRAS*, 428, 3183
- Epinat, B., Contini, T., Le Fèvre, O., et al. 2009, *A&A*, 504, 789
- Epinat, B., Tasca, B., Amram, P., et al. 2012, *A&A*, 539, A92
- Erb, D. K., Shapley, A. E., Steidel, C. C., et al. 2003, *ApJ*, 591, 101
- Förster Schreiber, N. M., Genzel, R., Bouché, N., et al. 2009, *ApJ*, 706, 1364
- Genzel, R., Schreiber, N. M. F., Übler, H., et al. 2017, *Nature*, 543, 397
- Hainline, L. J., Blain, A. W., Smail, I., et al. 2011, *ApJ*, 740, 96
- Kassin, S. A., de Jong, R. S., & Weiner, B. J. 2006, *ApJ*, 643, 804
- Kennicutt, Jr., R. C. 1998, *ARA&A*, 36, 189
- Koekemoer, A. M., Aussel, H., Calzetti, D., et al. 2007, *ApJS*, 172, 196
- Korsaga, M., Carignan, C., Amram, P., Epinat, B., & Jarrett, T. H. 2018, *MNRAS*, arXiv:1804.05820
- Laigle, C., McCracken, H. J., Ilbert, O., et al. 2016, *ApJS*, 224, 24
- Lang, P., Förster Schreiber, N. M., Genzel, R., et al. 2017, *ApJ*, 840, 92
- Law, D. R., Steidel, C. C., Erb, D. K., et al. 2009, *ApJ*, 697, 2057
- Lovell, M. R., Pillepich, A., Genel, S., et al. 2018, *ArXiv e-prints*, arXiv:1801.10170
- Martinsson, T. P. K., Verheijen, M. A. W., Westfall, K. B., et al. 2013a, *A&A*, 557, A131
- . 2013b, *A&A*, 557, A130
- McCracken, H. J., Milvang-Jensen, B., Dunlop, J., et al. 2012, *A&A*, 544, A156
- McGaugh, S. S. 2016, *ApJ*, 816, 42
- McLean, I. S., Steidel, C. C., Epps, H., et al. 2010, in *Proc. SPIE*, Vol. 7735, Ground-based and Airborne Instrumentation for Astronomy III, 77351E–77351E–12
- McLean, I. S., Steidel, C. C., Epps, H. W., et al. 2012, in *Proc. SPIE*, Vol. 8446, Ground-based and Airborne Instrumentation for Astronomy IV, 84460J
- Pelliccia, D., Tresse, L., Epinat, B., et al. 2017, *A&A*, 599, A25
- Peng, C. Y., Ho, L. C., Impey, C. D., & Rix, H.-W. 2002, *AJ*, 124, 266
- Planck Collaboration, Ade, P. A. R., Aghanim, N., et al. 2016, *A&A*, 594, A13
- Price, S. H., Kriek, M., Shapley, A. E., et al. 2016, *ApJ*, 819, 80
- Rubin, V. C., Burbridge, E. M., Burbidge, G. R., Crampin, D. J., & Prendergast, K. H. 1965, *ApJ*, 141, 759
- Rubin, V. C., Thonnard, N., & Ford, Jr., W. K. 1978, *ApJ*, 225, L107
- Salvatier, J., Wiecki, T. V., & Fonnesbeck, C. 2016, *PyMC3: Python probabilistic programming framework*, Astrophysics Source Code Library, ascl:1610.016
- Scoville, N., Sheth, K., Aussel, H., et al. 2016, *ApJ*, 820, 83
- Sérsic, J. L. 1963, *Boletín de la Asociacion Argentina de Astronomia La Plata Argentina*, 6, 41
- Simons, R. C., Kassin, S. A., Weiner, B. J., et al. 2017, *ApJ*, 843, 46
- Sofue, Y., & Rubin, V. C. 2001, *ARA&A*, 39, 137
- Stott, J. P., Swinbank, A. M., Johnson, H. L., et al. 2016, *MNRAS*, 457, 1888
- Swinbank, A. M., Smail, I., Chapman, S. C., et al. 2004, *ApJ*, 617, 64
- Teklu, A. F., Remus, R.-S., Dolag, K., et al. 2018, *ApJ*, 854, L28
- van Albada, T. S., Bahcall, J. N., Begeman, K., & Sancisi, R. 1985, *ApJ*, 295, 305
- van Starkenburg, L., van der Werf, P. P., Franx, M., et al. 2008, *A&A*, 488, 99
- Weiner, B. J., Willmer, C. N. A., Faber, S. M., et al. 2006, *ApJ*, 653, 1027
- White, S. D. M., & Rees, M. J. 1978, *MNRAS*, 183, 341
- Wisnioski, E., Förster Schreiber, N. M., Wuyts, S., et al. 2015, *ApJ*, 799, 209
- Wright, S. A., Larkin, J. E., Barczys, M., et al. 2007, *ApJ*, 658, 78

Wuyts, S., Förster Schreiber, N. M., Wisnioski, E., et al. 2016, ApJ, 831, 149

Xue, R., Fu, H., Isbell, J., et al. 2018, ArXiv e-prints, arXiv:1807.04291

Yuan, T., Richard, J., Gupta, A., et al. 2017, ApJ, 850, 61